Pressure-induced polymorphism in SrB_{6} and deformation mechanisms of covalent networks

Li Zhu, Gustav M. Borstad, R. E. Cohen, and Timothy A. Strobel

Phys. Rev. B **100**, 214102 — Published 4 December 2019

DOI: 10.1103/PhysRevB.100.214102

Pressure-Induced Polymorphism in SrB_6 and Deformation Mechanisms of Novel Covalent Networks

Li Zhu[1,*], Gustav M. Borstad[1], R. E. Cohen[1,2], and Timothy A. Strobel[1,†]

[1]*Geophysical Laboratory, Carnegie Institution for Science, 5251 Broad Branch Road, NW, Washington, DC 20015, USA*

[2]*Department of Earth and Environmental Sciences, Ludwig Maximilians Universität, Munich 80333, Germany*

* z@zhuli.name
† tstrobel@carnegiescience.edu

ABSTRACT

We study the high-pressure structures of SrB_6 up to 200 GPa using first-principles structure prediction calculations and high-pressure X-ray diffraction experiments. The computations show that the ambient-pressure cubic phase transforms to an orthorhombic structure (*Cmmm*) at 48 GPa, and then to a tetragonal structure (*I*4/*mmm*) at 60 GPa. The high-pressure experiments are consistent with the theoretically predicted tetragonal structure, which was quenched successfully to ambient conditions. Pressure induces simple boron octahedra to form complex networks in which the electrons are delocalized, leading to metallic ground states with large density of states at the Fermi level. Calculated stress-strain relations for the *I*4/*mmm* structure of SrB_6 demonstrate its intrinsic hard nature with an estimated Vickers hardness of 15 GPa, and reveal a novel deformation mechanism with transient multicenter bonding that results in the combination of high strength and high ductility. Our findings offer valuable insights for understanding the rich and complex crystal structures of SrB_6, which have broad implications for further explorations of hexaboride materials.

INTRODUCTION

Metal borides often exhibit fascinating structural complexity due to the electron deficient nature of boron that enables versatile polyhedral frameworks [1,2]. There are more than 200 binary metal borides that include a broad range of structural configurations, and many of them exhibit remarkable properties. For example, magnesium diboride (MgB_2) exhibits a substantial superconducting transition temperature with T_c = 39 K [3–9]. Among the metal borides, hexaboride materials have been the subject of intense experimental and theoretical study because of their technological and fundamental importance [10–20]. Some of the rare-earth hexaborides are excellent thermionic electron emission materials. For examples, CeB_6 exhibits Kondo behavior and valence-fluctuations [21], and LaB_6 has extremely high thermionic emission efficiency and used as an electron source [22]. Recently, superconductivity at 7 K was observed for YB_6 [23], while narrow-gap semiconducting behavior was found in YbB_6 [24]. Recent studies also show that SmB_6 and PuB_6 are strongly correlated topological insulators that have ideal solid-state properties for nuclear fuel materials [15,19]. Alkaline-earth metal hexaborides are also known for a range of excellent properties and applications. Boron-deficient MgB_6 exhibits the coexistence of weak ferromagnetism and antiferroelectricity [25]. Bulk CaB_6, SrB_6, and BaB_6 have very favorable Seebeck coefficients and electrical conductivities, with SrB_6 showing the highest power factor of the three [26].

At ambient conditions, most alkaline-earth metal hexaborides, MB_6 (M = Ca, Sr, Ba), crystallize in a cubic structure (space group: $Pm\bar{3}m$), which can be represented by B_6 octahedra and metal ions arranged in a CsCl-type lattice. However, structure searching methods combined with first-principles calculations [27] suggest that the ambient structure of MgB_6 [25,28] may be orthorhombic. High-pressure phases of alkaline-earth metal hexaborides have also motivated extensive studies. Pressure can efficiently reduce interatomic distances and modify electronic orbitals and bonding patterns, thus leading to the formation of novel materials with atypical physical properties. A recent high-pressure study on CaB_6 showed that the ambient $Pm\bar{3}m$ structure becomes unstable above 13 GPa, and several phase transitions occur under higher pressure [29]. In contrast to the rich phase transitions in CaB_6, BaB_6 was found to be surprisingly stable, and remains in the ambient-pressure structure up to at least 49 GPa [30]. Theoretical calculations show that BaB_6 may transform into several new high-pressure phases above 78

GPa [30]. SrB_6, a member of the rare-earth hexaborides family, has also fascinated scientists for many years owing to its mechanical and electronic properties, such as ultra-incompressibility [31] and thermopower [26,32]. Despite the possibility for many novel phases with enhanced functionality, the high-pressure structures of SrB_6 remain relatively unexplored. Here, we report the high-pressure phases of SrB_6 with a joint theoretical and experimental study. We first predicted the high-pressure phase diagram of SrB_6 using swarm-intelligence-based structure prediction methods [33,34]. The predictions indicate two phase transitions in SrB_6 which is found to follow a cubic-orthorhombic-tetragonal sequence. Powder X-ray diffraction measured at high pressure after heating SrB_6 at 2000 K can be indexed with the predicted tetragonal crystal structure. Further calculations reveal the deformation mechanism of the complex covalent network.

METHODS

Global structural optimization was performed using the CALYPSO code [33–35] with the particle swarm optimization algorithm, which has successfully predicted structures of various systems ranging from elements to binary and ternary compounds [36–42]. The energetic calculations were carried out using density functional theory within the Perdew-Burke-Ernzerh [43] generalized gradient approximation as implemented in the VASP code [44]. We used projector augmented waves (PAW) [45] with $4s^2 4p^6 5s^2$ and $2s^2 2p^1$ electrons as valence for Sr and B atoms, respectively. The electronic wave functions were expanded in a plane-wave basis set with a cutoff energy of 520 eV. Monkhorst-Pack *k*-point meshes [46] with a grid of spacing $0.04 \times 2\pi$ Å^{-1} for Brillouin zone sampling were chosen. To determine the dynamical stability of the studied structures, we performed phonon calculations by using the finite displacement approach, as implemented in the phonopy code [47]. Electron−phonon coupling calculations for superconducting properties of stable phases were performed using density-functional perturbation theory (DFPT) with the Quantum-ESPRESSO package [48]. The stress-strain relation was obtained by calculating the stress response to structural deformation along specific loading paths using a quasistatic relaxation method [49].

SrB_6 (EPSI Metals, 99.5 %) was purchased commercially and used without further purification. The SrB_6 powder was loaded in a diamond anvil cell (DAC) with 100 μm diameter

culets and a Re gasket within an inert Ar glovebox, and subsequently gas loaded using Ar [50] or Ne [51] pressure media. Powder X-ray diffraction (XRD) measurements were completed at the High-Pressure Collaborative Access Team (HPCAT) beamline 16-IDB, and GSECARS, beamline 13-IDD, at the Advanced Photon Source of Argonne National Laboratory. Calibration of the sample-to-detector distance was performed with a CeO_2 or LaB_6 standard and the DIOPTAS program [52]. After heating the sample above 2000 K using a double-sided infrared laser heating system, a monochromatic beam with $\lambda = 0.4066$ Å or $\lambda = 0.3344$ Å was focused on the sample, and diffraction data were recorded on an MARCCD or Pilatus 1M detector. The Le Bail fitting of the powder patterns were conducted using GSAS with EXPGUI [53].

RESULTS AND DISCUSSION

Structure prediction calculations were performed in the pressure range 0 – 200 GPa with up to four formula unit (f.u.) per simulation cell. Below 40 GPa, we found the most stable structure is the $Pm\bar{3}m$ phase, in agreement with experiment. We uncovered a group of new structures under high-pressure conditions. Among them, two lower-symmetry structures were found as ground state structures at different pressures. At 50 GPa, we predicted an orthorhombic structure described by space group *Cmmm* (4 f.u. per unit cell) as depicted in Fig. 1c. Above 60 GPa, we found that the most stable structure consists of a large 48-atom boron network within a tetragonal unit cell with the space group *I*4/*mmm*. Figure 1 shows the structural evolution with pressure, which can be viewed as a continuous distortion of B and Sr atoms. Pressure disrupts the original cubic phase to form denser structures with more complex boron networks. The basic building blocks of the SrB_6 phases are related to different kinds of boron polyhedra. As pressure increases, all boron octahedra in the $Pm\bar{3}m$ phase open up, fuse with the neighboring ones, and result in the formation of twinned pentagonal bipyramids in the *Cmmm* structure. On further compression, the boron atoms re-bond to a more complex network composed of twinned biaugmented triangular prisms (Fig. 1e). As driven by the need for denser structural packing, pressure also breaks the original line-arranged Sr atoms to form more compact configurations with Sr zigzag chains in the *I*4/*mmm* structure (Fig. 1e).

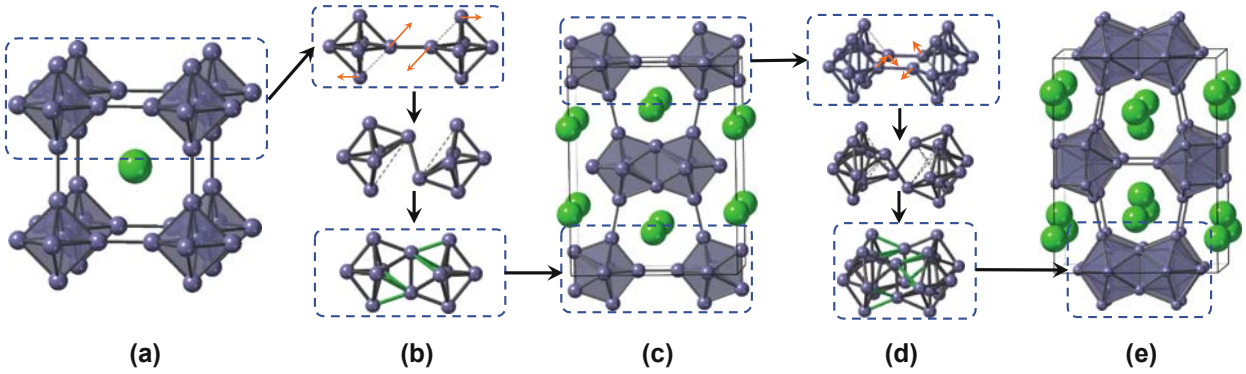

FIG. 1. Polyhedral views of (a) $Pm\bar{3}m$ structure, (c) *Cmmm* structure, and (e) *I*4/*mmm* structure of SrB_6. The phase transition mechanisms of (b) $Pm\bar{3}m \rightarrow$ *Cmmm* structure and (d) *Cmmm* $\rightarrow$ *I*4/*mmm* structure. The black lines denote the unit cells and large and small spheres represent Sr and B atoms, respectively.

The calculated enthalpy curves (relative to the $Pm\bar{3}m$ structure, Fig. 2) illustrate the relative thermodynamic stabilities of our predicted structures. Our results show that up to 48 GPa, the ambient $Pm\bar{3}m$ structure is the most stable one, and a pressure-induced phase transition from $Pm\bar{3}m$ to *Cmmm* occurs at ~48 GPa. The *Cmmm* phase is the most energetically favorable structure in a limited pressure range between 48 to 60 GPa. Beyond 60 GPa, the predicted *I*4/*mmm* structure becomes more stable up to at least 200 GPa. The phase transitions involve a complex evolution of the boron network in SrB_6 with the increasing pressure. To further understand the effect of pressure, we plot the enthalpy components (internal energy term and pressure-volume, pV, terms) of the *Cmmm* and *I*4/*mmm* phases relative to the $Pm\bar{3}m$ phase in Fig. 2b. The $Pm\bar{3}m$ structure has the lowest internal energy over the entire pressure range studied in this work. However, as pressure increases, the pV terms for the *Cmmm* and *I*4/*mmm* structures decrease quickly, and are large enough to compensate for the internal energy difference. Pressure plays an important role in shifting the stability of different structures and thus is a unique tool to create a high-coordination environment for novel materials. The dynamic stabilities of the newly predicted *Cmmm* and *I*4/*mmm* structures were examined by calculating the phonon spectra using the supercell method. No imaginary phonon frequencies were found in the whole Brillouin zone over the studied pressure range, indicating the dynamic stabilities and favorable conditions for metastable recovery to ambient pressure [54].

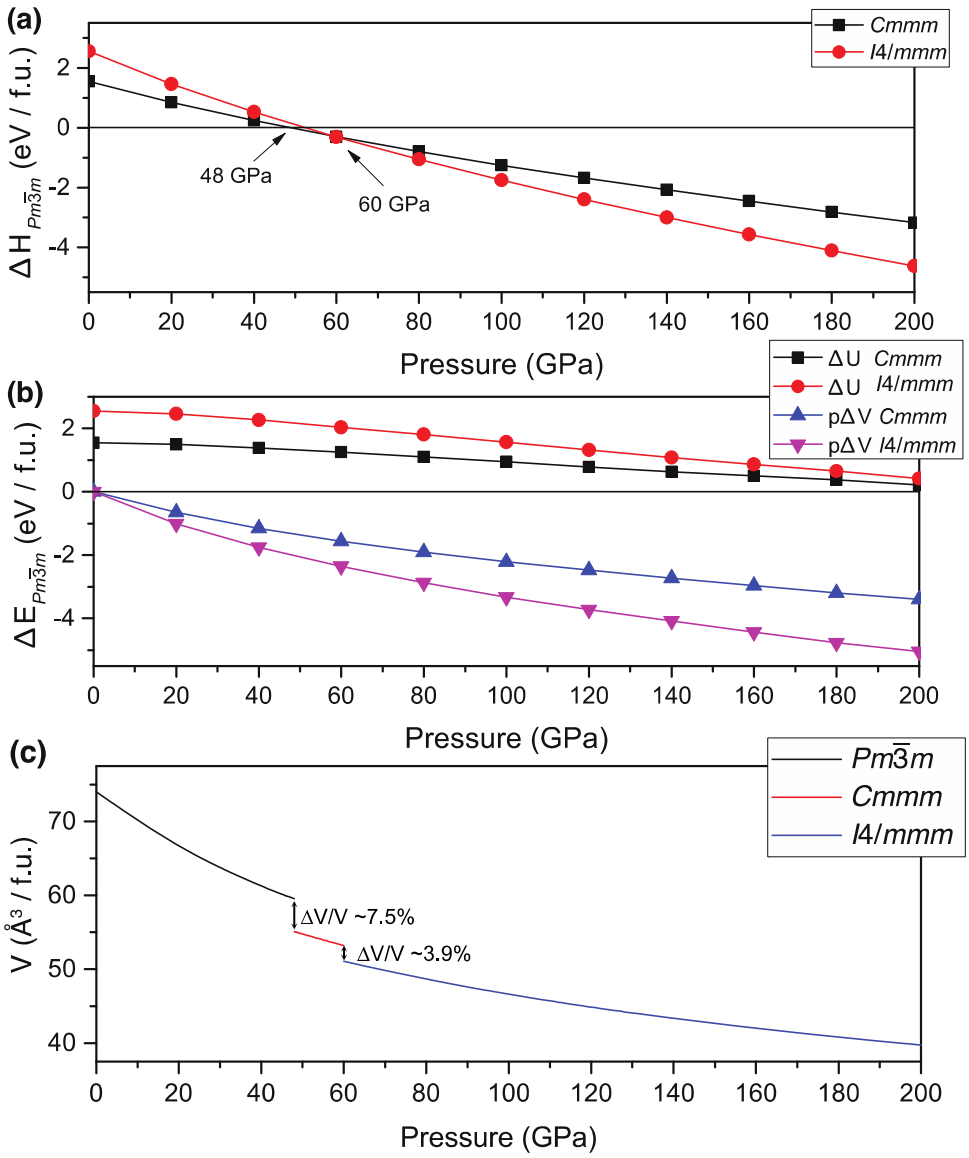

FIG. 2. (a) Calculated enthalpy curves for SrB_6 (relative to the $Pm\bar{3}m$ structure) as a function of pressure. (b) The relative internal energy ΔU and pΔV term for the *Cmmm* and *I*4/*mmm* structures with respect to the $Pm\bar{3}m$ structure. (c) Calculated volumes as a function of pressure for different phases of SrB_6.

In order to confirm the theoretically predicted phase transitions under high pressures, we performed high-pressure XRD experiments on SrB_6. Initial experiments performed near 60 GPa did not reveal the formation of new SrB_6 polymorphs, even after heating near 2000 K. This suggests either a significant kinetic barrier for the transition at 60 GPa, or means that the actual

transition pressures at finite temperature are higher than those calculated. It is very common that heating is needed to promote rebonding in the strongly bound covlanet network under high pressures [29,55]. For high-pressure experiments conducted with much higher thermodynamic driving force (near 150 GPa), cubic diffraction lines from $Pm\bar{3}m$ SrB_6 rapidly transformed to a series of new peaks, signifying the formation of a new high-pressure phase. The XRD patterns agree with the predicted tetrahedral *I*4/*mmm* structure as shown in Fig 3a, although the calculated peak intensities show some variation due to incomplete powder averaging statistics. We refined the lattice parmeters of the predicted I4/*mmm* structure with the observed XRD data obtained during decompression down to 1 atm, and the pressure-volume equation of state (EoS) is consistent with that calculated for the *I*4/*mmm* structure (Fig. 3b), providing further evidence for the formation of the *I*4/*mmm* phase of SrB_6. The experimental lattice parameters are given in the Supplemental Materials [54]. Compared with the cubic phase, the new tetragonal phase shows increased compressibility (estimated experimental B_0 = 148(6) GPa compared with B_0 = 123 GPa for the cubic phase), and an overall decrease in volume per formula unit due to the increased connectivity of the boron biaugmented triangular prisms compared with the pristine octahedra.

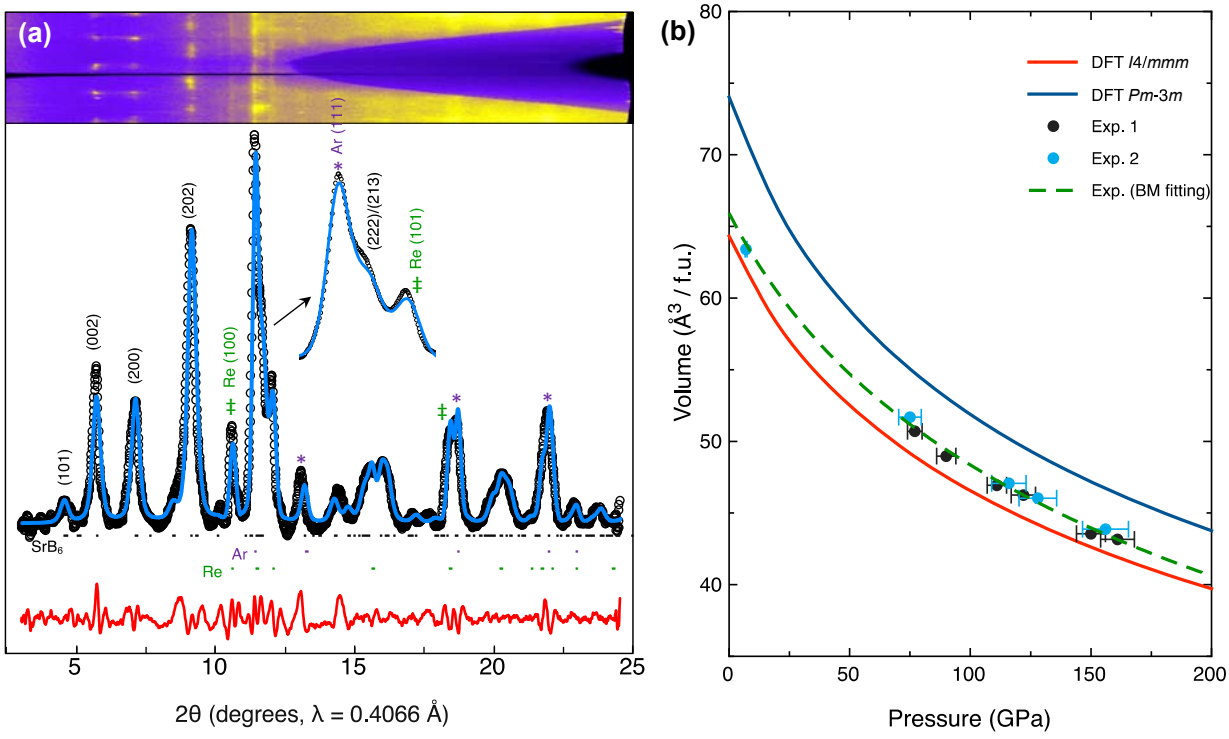

FIG. 3. X-ray diffraction and equation of state of the *I*4/*mmm* structure of SrB_6. (a) Experimental XRD data (black points) collected at 159(9) GPa with Le Bail fitting (blue line). Green and purple ticks (and selected Bragg reflections) indicate contributions from Re and Ar, respectively. The upper panel shows the cake-type image of the two-dimensional XRD pattern with incomplete powder averaging. (b) Experimental pV data for *I*4/*mmm* SrB_6 are shown as points, and the solid line is the theoretical result (GGA PBE). The estimated error in volume is smaller than the symbol size. The pV data were fitted using the second order Birch-Murnaghan EoS [56], and the estimated experimental bulk modulus B_0 = 148(6) GPa is consistent with the calculated B_0 = 152 GPa for *I*4/*mmm* SrB_6. The calculated EoS with B_0 = 123 GPa for cubic SrB_6 is shown for comparison.

The high-pressure phase behavior of SrB_6 shares similarities with that of CaB_6 [29]. Both compounds take on the cubic $Pm\bar{3}m$ structure at low pressure and transform to the tetragonal *I*4/*mmm* structure at high pressure. The calculated transition pressure for *I*4/*mmm* CaB_6 is 32 GPa, whereas that of SrB_6 is 60 GPa. While experimental evidence for the CaB_6 transition was observed at 31 GPa, significantly higher pressure was required for SrB_6. A possible explanation for this is related to the stability of the M-point phonon frequency for the cubic phase, which persists to higher pressure monotonically with increasing cation mass [29]. There are also noteworthy differences in the predicted phase transition sequences for CaB_6 and SrB_6. For the case of CaB_6, the cubic phase is predicted to first transform to an orthorhombic structure with 28 atoms per cell (*Cmmm*) at 13 GPa, then a second orthorhombic structure with 56 atoms per cell (*Cmcm*), before finally reaching the tetragonal structure at 32 GPa. For the case of SrB_6, we predict only the *Cmmm* orthorhombic structure as an intermediate phase between a narrow pressure window of 48-60 GPa. None of the orthorhombic strucutures for CaB_6 or SrB_6 were successfully confirmed by experiment, which could be related to their limited range of stability or differences in energetics at finite temperature.

The high-pressure polymorphs of SrB_6 reveal the rich chemistry of B, enabling the formation of various kinds of unique polyhedra. Under pressure, the enthalpies and volumes decrease as a result of additional B-B bonds, which increases the overall widths of the valence and conduction bands. A sufficiently large bandwidth expansion will force valence and conduction bands to overlap at the Fermi level, leading to metallic behavior. To investigate the

electronic properties, we calculated the projected density of states (DOS) for the three structures of SrB_6, as shown in Fig. 4. The modified Becke-Johnson type of meta GGA was used here to obtain band gaps with an accuracy similar to hybrid functional or GW methods [57,58]. The DOS around the Fermi level is dominated by the B *p* and Sr *d* orbitals for all structures, with no Sr *s* component, indicating that the 5*s* electrons of Sr are entirely transfered to the boron networks. At ambient pressure, SrB_6 is a semiconductor with a band gap of around 1.1 eV (Fig. 5a), which is consistent with the experimentally measured optical band gap of 1.15±0.01 eV [13]. As the localized B_6 octahedra in the $Pm\bar{3}m$ structure transform to more extended edge-sharing polyhedra in the *Cmmm* and *I*4/*mmm* structures, electrons tend to become more delocalized. This electron delocalization is significant enough to induce metallic states for the *Cmmm* and *I*4/*mmm* structures (Fig. 5). This observation is in line with other boron compounds where metallicity increases when boron edge-sharing polyhedra are formed at the expense of inter-cluster bonds [27]. It is clear that the calculated densities of states at the Fermi level increase with elevated pressures, implying enhanced metallicity, which potentially sets a favorable condition for superconductivity. Metal borides, such as MgB_2 [3] and YB_6 [23], were reported to exhibit superconductivity. In this study, we find that the DOS at the Fermi level in the *Cmmm* and *I*4/*mmm* structures of SrB_6 are substantial, which suggests that the electron-phonon coupling could be large. We therefore estimated the superconducting transition temperature, T_c, from the Allen-Dynes modified McMillan equation [59]. With a Colomb potential (μ^*) of 0.1, giving an estimated T_c value of 9 K at 1 atm.

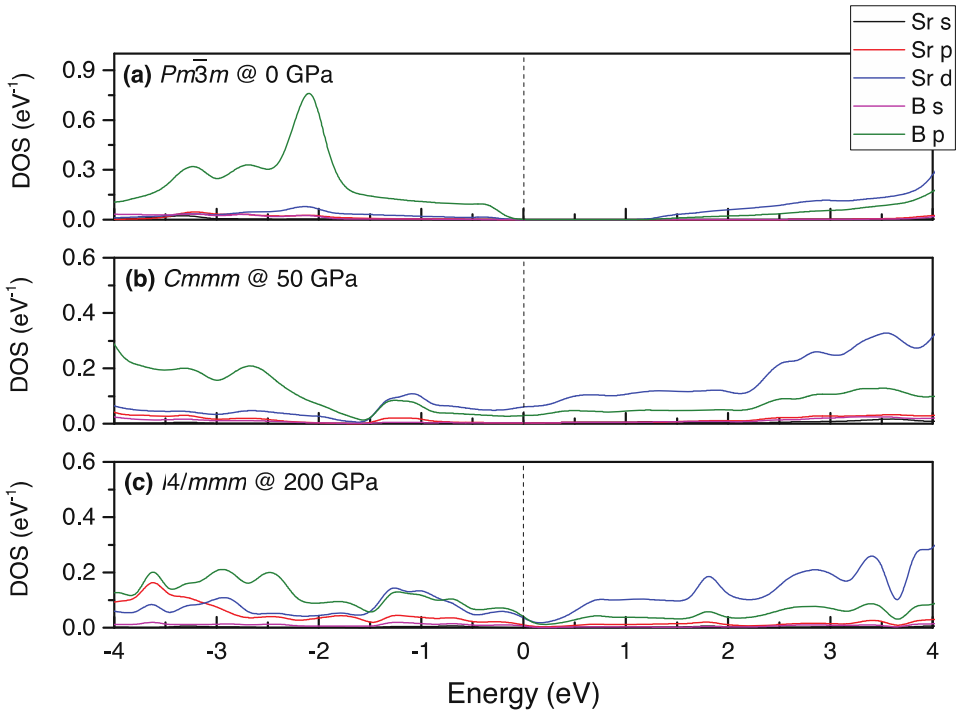

FIG. 4. The projected density of states (DOS) for (a) the $Pm\bar{3}m$ structure at 0 GPa, (b) the *Cmmm* structure at 50 GPa, and (c) the *I*4/*mmm* structure at 200 GPa. The densities of states at the Fermi level increase with pressure, indicating enhanced metallicity.

Borides are expected to be very hard. The increase in valence electron density from metallic elements can contribute to the strong covalent network, thereby enhancing the incompressibility of metal borides. The Vickers hardness for *I*4/*mmm* SrB6 was emstimated to be 19 GPa by using the microscopic hardness model [60]. We also determined the stress-strain relations for the recoverable *I*4/*mmm* structure of SrB_6 along different crystallographic directions, which provides insights into the local bond deformation mechanisms that establish key benchmarks for the intrinsic mechanical properties of a material. The calculated peak stresses provide a comprehensive and quantitative understanding of the value, range, and trend of the stress response under each type of strain. Tensile stresses along high-symmetry directions are first examined to find the weakest tensile directions that determine the easy cleavage planes. As shown in Fig. 5a, we can find that the *I*4/*mmm* structure has strong stress responses in the <001>, <110>, <111> and <101> directions with a peak tensile stress between 21 and 27 GPa. The weakest tensile direction is along the <100> direction with an ideal strength of 15 GPa, and thus the (100) planes represent the easy cleavage planes. Structural snapshots (Fig. 5c) show that the

boron bonds between the two biaugmented triangular prisms are the main load-bearing component where significant B-B stretching and breaking occurs under large tensile strain. To investigate the nature of bonding states, we plot the 2D electron localization function (ELF) for the key snapshots of *I*4/*mmm* SrB_6 under several critical tensile (T) and shear (S) strains (Fig. 5c). The covalent bonding nature of B_1-B_2 (1.81 Å) bonds is clearly visible at equilibrium (T0). As the tensile deformation along the <100> direction increases, the B_1-B_2 bond is continuously stretched and eventually broken when the tensile strain reaches $\epsilon = 0.08$ (T1). The calculated ELF shows localized electrons separated by a clear gap, indicating bond breakage.

We next evaluate the shear stress response in the (100) "easy cleavage planes" of SrB_6, and an ideal shear strength of 21 GPa is obtained in the (100)<011> shear direction (Fig. 5b). Intriguingly, our calculations reveal that the ideal shear strength first experiences a small drop and then increases quickly when the shear strain achieves $\epsilon = 0.13$ (S1) in the (100)<011> shear direction. These results point to unusual bonding characteristics in the *I*4/*mmm* structure of SrB_6. To examine the nature of these bonding states, we further plot the ELF for the structural snapshots at several critical shear-stress strains (Fig. 5c). With the increase of the shear deformation in the (100)<011> direction, the B_3-B_4 bond continuously stretches and becomes weaker, resulting in a small decrease of the shear strength at S1. We also found that the bond length of B_4-B_5 decreases while that of B_3-B_4 increases, accompanying charge transfer from the B_3-B_4 bond to the center of an interesting three-center bond ($\Delta B_3B_4B_5$). The strong three-center covalent bonding makes the structure stronger with high ductility and it undergoes a second elastic response regime until the shear strain reaches $\epsilon = 0.29$ (S3), resulting in a high peak stress of 22 GPa. This ductility and extended elastic behavior is in stark contrast to the results for other borides, e.g., the bonds break simultaneously at the peak strain with a precipitous drop in FeB_4 [61]. Once the shear strain reaches $\epsilon = 0.3$ (S4), the three-center bond of $\Delta B_3B_4B_5$ collapses, eventually causing structural deformation. The B_3-B_4 bond length drastically changes to 3.03 Å, and there are no localized electrons between the B_3 and B_4 atoms. These ideal strength results suggest a theoretical hardness of 15 GPa for the quenched *I*4/*mmm* structure of SrB_6. The multicenter bonding transition produces a simultaneously high-strength and high-ductility state in *I*4/*mmm* SrB_6, making it suitable candidate for various applications, such as for cutting, drawing, and rolling.

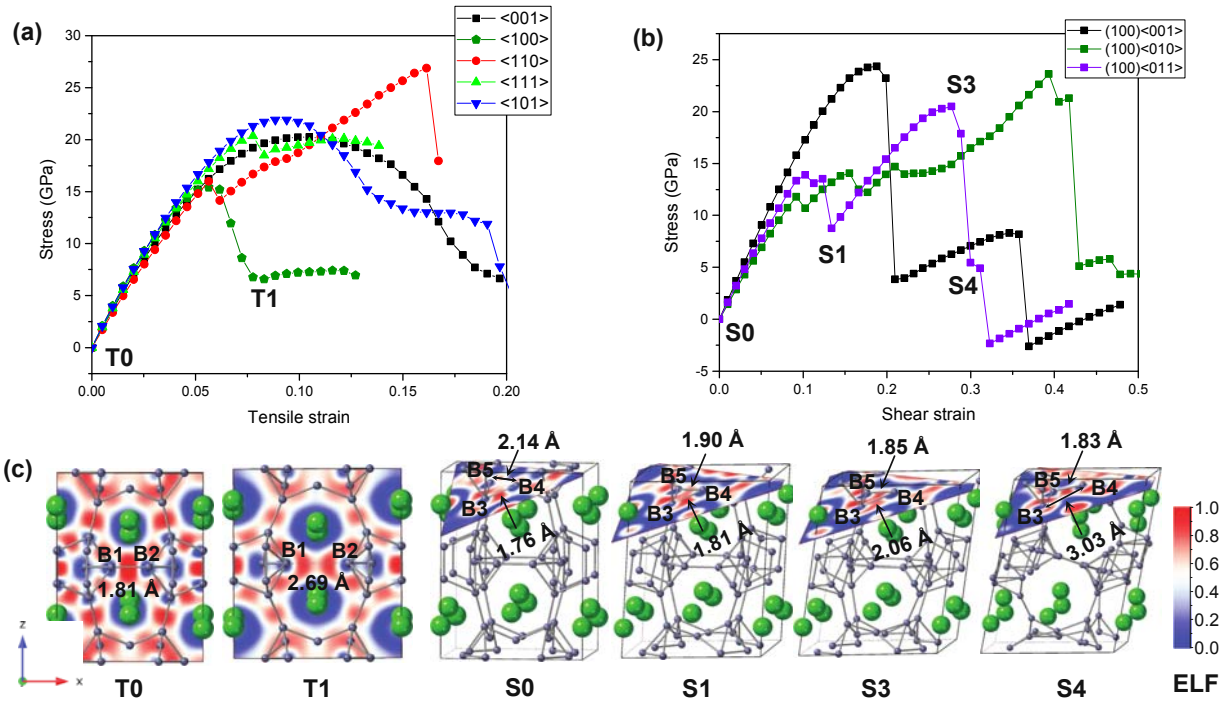

FIG. 5. (a) Calculated tensile stress-strain relations for the *I*4/*mmm* structure. (b) Calculated shear stress-strain relations for the *I*4/*mmm* structure in the (100) easiest cleavage plane. (c) 2D electron localization function (ELF) for the key structural snapshots of the *I*4/*mmm* structure in the tensile and shear directions. The small and large balls represent B and Sr atoms, respectively.

CONCLUSION

We combined automatic structure searching methods with first-principles calculations to investigate the high-pressure phase behavior, and electronic / mechanical properties of crystalline SrB_6. We identified two new high-pressure phases of SrB_6 that exhibit complex B covalent networks. Under high pressure, the ambient-pressure $Pm\bar{3}m$ structure of SrB_6 is first predicted to transform into the *Cmmm* structure with the formation of a boron framework comprised of twinned pentagonal bipyramids. At higher pressure, SrB_6 develops a more complex network composed of twinned biaugmented triangular prisms in the *I*4/*mmm* phase. The experimental XRD results are consistent with the predicted *I*4/*mmm* structure, and the high-pressure phase was successfully recovered to ambient conditions. Our calculations suggest that the *I*4/*mmm* structure of SrB_6 exhibits excellent mechanical behavior through a subtle quantum effect, which introduces the formation of three-center boron bonds from two-center bonds via continuous

charge transfer under shear stain. This unique behavior makes the *I*4/*mmm* structure of SrB_6 promising as a material for applications that require conventially "decoupled properties" due to the combination of high strength and enhanced ductility under shear strain. This work represents a significant step forward in understanding the high-pressure phase diagram of SrB_6, and the results obtained will provide insight and guidance to future studies on other borides.

ACKNOWLEDGEMENTS

This work was supported by DARPA under Grant No. W31P4Q1310005. Computations were carried out at the supercomputer Copper of DoD HPCMP Open Research Systems under project No. ACOMM35963RC1 and the Memex cluster of Carnegie Institution for Science. REC was also supported by the European Research Council Advanced Grant ToMCaT.

Reference

[1] S. Hermanek, Chem. Rev. **92**, 175 (1992).
[2] X.-L. He, X. Dong, Q. Wu, Z. Zhao, Q. Zhu, A. R. Oganov, Y. Tian, D. Yu, X.-F. Zhou, and H.-T. Wang, Phys. Rev. B **97**, 100102 (2018).
[3] J. Nagamatsu, N. Nakagawa, T. Muranaka, Y. Zenitani, and J. Akimitsu, Nature **410**, 63 (2001).
[4] J. Kortus, I. I. Mazin, K. D. Belashchenko, V. P. Antropov, and L. L. Boyer, Phys. Rev. Lett. **86**, 4656 (2001).
[5] C. Buzea and T. Yamashita, Supercond. Sci. Technol. **14**, R115 (2001).
[6] D. C. Larbalestier, L. D. Cooley, M. O. Rikel, A. A. Polyanskii, J. Jiang, S. Patnaik, X. Y. Cai, D. M. Feldmann, A. Gurevich, A. A. Squitieri, M. T. Naus, C. B. Eom, E. E. Hellstrom, R. J. Cava, K. A. Regan, N. Rogado, M. A. Hayward, T. He, J. S. Slusky, P. Khalifah, K. Inumaru, and M. Haas, Nature **410**, 186 (2001).
[7] H. J. Choi, D. Roundy, H. Sun, M. L. Cohen, and S. G. Louie, Nature **418**, 758 (2002).
[8] Y. Ma, Y. Wang, and A. R. Oganov, Phys. Rev. B **79**, 054101 (2009).
[9] P. Ravindran, P. Vajeeston, R. Vidya, A. Kjekshus, and H. Fjellvåg, Phys. Rev. B **64**, 224509 (2001).
[10] Z.-G. Li, C.-G. Piao, X. Pan, Y.-K. Wei, Y. Cheng, and G.-F. Ji, Phys. B Condens. Matter **407**, 361 (2012).
[11] B. Amsler, Z. Fisk, J. L. Sarrao, S. von Molnar, M. W. Meisel, and F. Sharifi, Phys. Rev. B **57**, 8747 (1998).
[12] S. Xu, F. Jia, Y. Yang, L. Qiao, S. Hu, D. J. Singh, and W. Ren, Phys. Rev. B **100**, 104408 (2019).

[13] J. D. Denlinger, J. A. Clack, J. W. Allen, G.-H. Gweon, D. M. Poirier, C. G. Olson, J. L. Sarrao, A. D. Bianchi, and Z. Fisk, Phys. Rev. Lett. **89**, 157601 (2002).
[14] S. Massidda, A. Continenza, T. M. de Pascale, and R. Monnier, Zeitschrift Für Phys. B Condens. Matter **102**, 83 (1996).
[15] D. J. Kim, J. Xia, and Z. Fisk, Nat. Mater. **13**, 466 (2014).
[16] H. Ahmed and A. N. Broers, J. Appl. Phys. **43**, 2185 (1972).
[17] R. Monnier and B. Delley, Phys. Rev. Lett. **87**, 157204 (2001).
[18] J. R. Brewer, N. Deo, Y. Morris Wang, and C. L. Cheung, Chem. Mater. **19**, 6379 (2007).
[19] X. Deng, K. Haule, and G. Kotliar, Phys. Rev. Lett. **111**, 176404 (2013).
[20] J. Wang, X. Song, X. Shao, B. Gao, Q. Li, and Y. Ma, J. Phys. Chem. C **122**, 27820 (2018).
[21] W. Joss, J. M. van Ruitenbeek, G. W. Crabtree, J. L. Tholence, A. P. J. van Deursen, and Z. Fisk, Phys. Rev. Lett. **59**, 1609 (1987).
[22] X. H. Ji, Q. Y. Zhang, J. Q. Xu, and Y. M. Zhao, Prog. Solid State Chem. **39**, 51 (2011).
[23] Y. Xu, L. Zhang, T. Cui, Y. Li, Y. Xie, W. Yu, Y. Ma, and G. Zou, Phys. Rev. B **76**, 214103 (2007).
[24] J. M. Tarascon, J. Etourneau, P. Dordor, P. Hagenmuller, M. Kasaya, and J. M. D. Coey, J. Appl. Phys. **51**, 574 (1980).
[25] I. Popov, N. Baadji, and S. Sanvito, Phys. Rev. Lett. **108**, 107205 (2012).
[26] M. Takeda, M. Terui, N. Takahashi, and N. Ueda, J. Solid State Chem. **179**, 2823 (2006).
[27] H. Wang, K. A. LeBlanc, B. Gao, and Y. Yao, J. Chem. Phys. **140**, 044710 (2014).
[28] S. Li, O. Prabhakar, T. T. Tan, C. Q. Sun, X. L. Wang, S. Soltanian, J. Horvat, and S. X. Dou, Appl. Phys. Lett. **81**, 874 (2002).
[29] A. N. Kolmogorov, S. Shah, E. R. Margine, A. K. Kleppe, and A. P. Jephcoat, Phys. Rev. Lett. **109**, 75501 (2012).
[30] X. Li, X. Huang, D. Duan, G. Wu, M. Liu, Q. Zhuang, S. Wei, Y. Huang, F. Li, Q. Zhou, B. Liu, and T. Cui, RSC Adv. **6**, 18077 (2016).
[31] S. Xin, S. Liu, N. Wang, X. Han, L. Wang, B. Xu, Y. Tian, Z. Liu, J. He, and D. Yu, J. Alloys Compd. **509**, 7927 (2011).
[32] M. Takeda, T. Fukuda, F. Domingo, and T. Miura, J. Solid State Chem. **177**, 471 (2004).
[33] Y. Wang, J. Lv, L. Zhu, and Y. Ma, Phys. Rev. B **82**, 94116 (2010).
[34] Y. Wang, J. Lv, L. Zhu, and Y. Ma, Comput. Phys. Commun. **183**, 2063 (2012).
[35] B. Gao, P. Gao, S. Lu, J. Lv, Y. Wang, and Y. Ma, Sci. Bull. **64**, 301 (2019).
[36] Y. Wang, H. Liu, J. Lv, L. Zhu, H. Wang, and Y. Ma, Nat. Commun. **2**, 563 (2011).
[37] L. Zhu, Z. Wang, Y. Wang, G. Zou, H. Mao, and Y. Ma, Proc. Natl. Acad. Sci. U.S.A. **109**, 751 (2012).
[38] J. Lv, Y. Wang, L. Zhu, and Y. Ma, Phys. Rev. Lett. **106**, 15503 (2011).
[39] Y. Wang, J. Lv, L. Zhu, S. Lu, K. Yin, Q. Li, H. Wang, L. Zhang, and Y. Ma, J. Phys. Condens. Matter **27**, 203203 (2015).
[40] L. Zhu, H. Wang, Y. Wang, J. Lv, Y. Ma, Q. Cui, Y. Ma, and G. Zou, Phys. Rev. Lett. **106**, 145501 (2011).
[41] L. Zhu, H. Liu, C. J. Pickard, G. Zou, and Y. Ma, Nat. Chem. **6**, 644 (2014).
[42] S. Zhang, L. Zhu, H. Liu, and G. Yang, Inorg. Chem. **55**, 11434 (2016).
[43] J. P. Perdew, K. Burke, and M. Ernzerhof, Phys. Rev. Lett. **77**, 3865 (1996).
[44] G. Kresse and J. Furthmüller, Phys. Rev. B **54**, 11169 (1996).
[45] P. E. Blöchl, Phys. Rev. B **50**, 17953 (1994).

[46] H. J. Monkhorst and J. D. Pack, Phys. Rev. B **13**, 5188 (1976).
[47] A. Togo and I. Tanaka, Scr. Mater. **108**, 1 (2015).
[48] P. Giannozzi, S. Baroni, N. Bonini, M. Calandra, R. Car, C. Cavazzoni, D. Ceresoli, G. L. Chiarotti, M. Cococcioni, I. Dabo, A. Dal Corso, S. de Gironcoli, S. Fabris, G. Fratesi, R. Gebauer, U. Gerstmann, C. Gougoussis, A. Kokalj, M. Lazzeri, L. Martin-Samos, N. Marzari, F. Mauri, R. Mazzarello, S. Paolini, A. Pasquarello, L. Paulatto, C. Sbraccia, S. Scandolo, G. Sclauzero, A. P. Seitsonen, A. Smogunov, P. Umari, and R. M. Wentzcovitch, J. Phys. Condens. Matter **21**, 395502 (2009).
[49] D. Roundy, C. R. Krenn, M. L. Cohen, and J. W. Morris, Phys. Rev. Lett. **82**, 2713 (1999).
[50] D. Errandonea, R. Boehler, S. Japel, M. Mezouar, and L. R. Benedetti, Phys. Rev. B **73**, 092106 (2006).
[51] A. Dewaele, F. Datchi, P. Loubeyre, and M. Mezouar, Phys. Rev. B **77**, 094106 (2008).
[52] C. Prescher and V. B. Prakapenka, High Press. Res. **35**, 223 (2015).
[53] B. H. Toby, J. Appl. Crystallogr. **34**, 210 (2001).
[54] See Supplemental Material at [URL] for additional details on experiment and calculation.
[55] D. Laniel, G. Geneste, G. Weck, M. Mezouar, and P. Loubeyre, Phys. Rev. Lett. **122**, 066001 (2019).
[56] F. Birch, J. Geophys. Res. **57**, 227 (1952).
[57] A. D. Becke and E. R. Johnson, J. Chem. Phys. **124**, 221101 (2006).
[58] F. Tran and P. Blaha, Phys. Rev. Lett. **102**, 226401 (2009).
[59] P. B. Allen and R. C. Dynes, Phys. Rev. B **12**, 905 (1975).
[60] X. Guo, L. Li, Z. Liu, D. Yu, J. He, R. Liu, B. Xu, Y. Tian, and H.-T. Wang, J. Appl. Phys. **104**, 023503 (2008).
[61] M. Zhang, M. Lu, Y. Du, L. Gao, C. Lu, and H. Liu, J. Chem. Phys. **140**, (2014).